

Chapter 7

Characterization

In this chapter, important methods for the characterization of materials and surfaces, and in particular of thin films and nanostructures, will be presented. This is an integral part of the entire field, since it is by no means obvious that the growth and preparation discussed in the Chapter “Preparation” does indeed lead to the desired results, making careful and thorough characterization mandatory.

It turns out that for the complex structures in many cases it is advantageous to have a broad range of characterization techniques, which frequently are complementary to each other.

We shall organize these into

- scattering
- spectroscopy
- microscopy.

We emphasize that this section is not a replacement of specialized courses on these techniques. We rather present typical examples and strategies on how to employ them to characterize nanostructures, which means as a minimum requirement that we confirm that our preparation was successful.

We remark that the distinction of the above three categories is not infinitely strict, since also combinations of different techniques can be employed, such as, e.g., nano-diffraction, i.e. the combination of scattering with a very small beam, meaning diffraction data with lateral (microscopic) resolution or also nano-spectroscopy.

For scattering, we will focus mostly on grazing-incidence techniques, which make X-rays and neutrons ‘surface-sensitive’, for the characterization of the as-grown structures. Since scattering techniques are non-invasive and do not require instrumentation to be physically very close to the sample, which might interfere with the growth process, they can be employed *in situ*, i.e. for monitoring the growth process *in real time* with direct access to kinetic processes. We shall briefly outline the rather special role of these time-dependent scattering techniques, which are crucial in determining transient structures, i.e. structures that appear during the growth process, but only as intermediates, which are converted and disappear in the final sample, although they are crucial for its structure.

The area of spectroscopy is, of course, also rather broad, and comprises a large number of very different techniques. We shall give examples of some of these, which contribute

to characterizing growth and preparation techniques. In this context, element-specific techniques such as X-ray photoelectron spectroscopy (XPS) are unique in that they provide information on the elemental composition of the sample, including purity. Also spectroscopic techniques, at least some of them, can be employed in a time-dependent mode, i.e. during growth, so that the spectra can be followed as the sample is changing and the nanostructure is forming.

Microscopy techniques are being employed to create “images” of nanostructures, i.e. spatially resolved information that results from some type of physical interaction between a probe and an investigated nanostructure. Here our most commonly used strategy for image formation, the interaction between visible light and an object, reaches its limits, since the resolution is fundamentally restricted by the diffraction limit (about half the wavelength). The dimensions of nanostructures, and in particular the details of their shapes, are clearly smaller than that, therefore regular optical microscopy is not suited for their imaging. We will discuss different techniques with probes that are capable of higher resolution imaging, in particular focused electron beams (scanning and transmission electron microscopy), focused ion beams (ion microscopy), and a variety of scanning probes (e.g. scanning tunneling, atomic force, and scanning near-field optical microscopy). The respective interaction mechanisms, which are crucial for understanding what one “sees” in the images, will be analyzed, and exemplary images will be shown.

7.1 Scattering Methods

Sources:

- J. A. Venables, Introduction to Surface and Thin Film Processes,
H. Lüth, Surfaces and Interfaces of Solids (Springer 1993)
Auciello/Krauss, In-situ real-time characterization of thin films, Wiley
Als-Nielsen/McMorrow, Elements of Modern X-ray Physics, Wiley
H. Dosch, Critical Phenomena and Surfaces and Interfaces, Springer*

Concepts There are numerous ways to characterize thin films and nanostructures by scattering. Generally, the concepts discussed for scattering in 'BM KoMa' of course apply also for 'BM Nano'. For details we refer to specialized courses. Here, we will not review all of these, but rather point out a few issues specific for BM Nano.

In principle, any probe with wave-character may be considered, but since the typical length scale on the atomic level is Angstroms, we shall consider here only scattering probes with that wavelength. For probes with a rest mass we have

$$\lambda_{neutron}[\text{\AA}] = \frac{9.04}{\sqrt{E(\text{meV})}} = \sqrt{\frac{81.7}{E(\text{meV})}} \quad (7.1)$$

$$\lambda_{electron}[\text{\AA}] = \frac{11.85}{\sqrt{E(\text{eV})}} = \sqrt{\frac{140.4}{E(\text{eV})}} \quad (7.2)$$

$$\lambda_{^{40}Ar}[\text{\AA}] = \frac{4.5}{\sqrt{E(\text{meV})}} = \sqrt{\frac{20.4}{E(\text{meV})}} \quad (7.3)$$

$$\lambda_{xray}[\text{\AA}] = \frac{1.4}{\sqrt{E(\text{keV})}} = \sqrt{\frac{2.04}{E(\text{keV})}} \quad (7.4)$$

For photons, the relationship is

$$\lambda_{xray}[\text{\AA}] = \frac{12.4}{E[\text{keV}]} \quad (7.5)$$

Single-scattering approximation ('kinematic approximation') and Fourier transform

In the following, we shall focus on X-ray and neutron scattering, since these data are typically simpler to interpret due to the weaker (and frequently negligible) impact of multiple scattering. In fact, the applicability of the single-scattering approximation is the reason for the direct connection between the scattering signal $S(q)$ and the Fourier transform (FT) of the real-space structure, i.e. the distribution of material $\rho(x,y,z)$

$$S(q) \sim FT[\rho(x, y, z)] \quad (7.6)$$

Note that this is not limited to crystalline materials and the resulting reciprocal lattice, but applies also to non-crystalline materials or nanostructures with nanoparticles or quantum dots arranged in a possibly artificial arrangement (see examples).

7.1.1 Real time X-ray scattering during crystal growth

A particularly useful feature of scattering techniques is their applicability in real time, i.e. '*in situ*' during a process, while something is happening. This may be a chemical reaction, as is very popular and intriguing for catalysis studies and their kinetics, or oxidation of the surface, or the growth of a nanostructure itself.

In principle, all techniques above are applicable in real time, and these studies are then very important tests of growth models, as discussed in the previous Section.

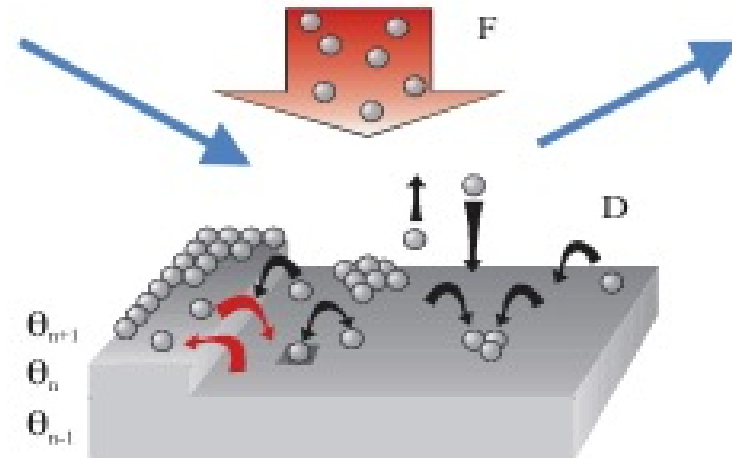


Fig. 7.1: Schematic of a scattering experiment *during* growth, i.e. in *real time* and *in situ*

In addition to applying the above 'regular' techniques, further specific techniques for real-time scattering have been developed.

A particularly nice and intriguing technique uses the scattering at the 'anti-Bragg point', where $q = \frac{\pi}{d}$ i.e. we have destructive interference of the scattering from neighboring lattice planes. For an infinitely extended bulk crystal, this would not result in any useful signal. For growth with time-dependent coverages $\theta_n(t)$ of these layers the time-dependence of the signal can be exploited to deduce information about the interference between (neighboring) odd and even layers and thus the growth process, as seen from

$$I_{reflected}(t) = \left| \sum_n f(q) \cdot \theta_n(t) \cdot e^{inqd} \right|^2 \quad (7.7)$$

$$I_{anti-Bragg}(t) = \left| \sum_n f(\pi/d_{film}) \cdot \theta_n(t) \cdot e^{in \cdot \frac{\pi}{d_{film}} \cdot d_{film}} \right|^2 \propto |\theta_1(t) - \theta_2(t) + \theta_3(t) - \dots|^2 \quad (7.8)$$

From the types of oscillations (or their absence) we can deduce information on the growth mode, e.g.

- unattenuated oscillations (see figure below)
→ layer-by-layer growth
- attenuation of the oscillations in a certain characteristic way
→ deviations from layer-by-layer growth (e.g., statistical growth)

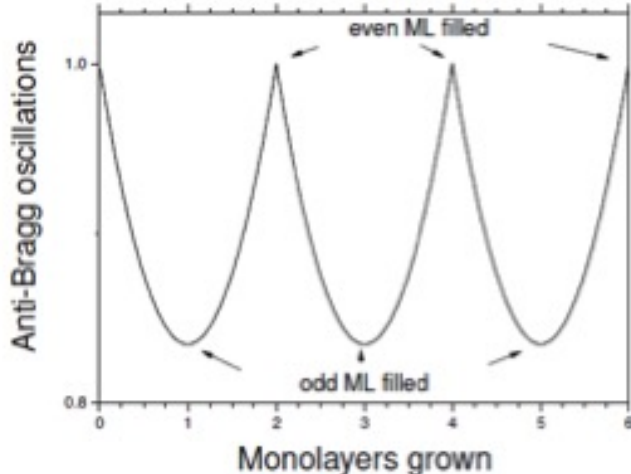


Fig. 7.2: Oscillations at the anti-Bragg point for the case of perfect layer-by-layer growth. Every 2 ML the signal recovers exactly to where it was before.

7.1.2 Size-related effects in scattering

The Bragg peak for an infinite crystal can be described by a delta-function, i.e. it has zero width (at least in the kinematical approximation). In practice, the width of the Bragg reflection is finite due to the finite resolution of experimental instrument. But there is also a fundamental effect, known as Scherrer broadening, which can be described by the Scherrer equation

$$\Delta(2\theta) = \frac{K \cdot \lambda}{D \cdot \cos \theta}. \quad (7.9)$$

Here $\Delta(2\theta)$ is the width of the Bragg peak (measured in the units of the scattering angle 2θ), λ is the wavelength, θ is the scattering angle, and $K \sim 1$ is a dimensionless coefficient which depends on the shape of the crystal. This equation describes broadening of the Bragg peak and it predicts that the Bragg reflections from small nanoparticles (or thin films) will be broader than the corresponding peaks from large crystals.

One can also write this equation in terms of the scattering vector (and not the scattering angle)

$$\Delta q = \frac{2\pi \cdot K}{D}. \quad (7.10)$$

7.1.3 Surface sensitivity and penetration depth

The penetration depth and thus the information depth and also the degree of 'surface sensitivity' differs substantially for the different probes. Very coarse estimates for normal incidence, obviously strongly dependent on the material, give (for $\lambda = 1 \text{ \AA}$)

Electrons	140 eV	$\sim 10 \text{ \AA}$
X-rays	12.4 keV	$\sim 50 \text{ mm}$
Neutrons	81 meV	$\sim 1 \text{ cm}$

Helium or Argon atoms at thermal energies (i.e. $\lambda \sim 1 \text{ \AA}$, not to be confused with ions accelerated in an electrical field) do not penetrate a surface and have thus perfect surface sensitivity. They are slightly less common, though, and we refer to specialized literature.

Electrons exhibit an intrinsically small penetration depth at the above energies due to their strong interaction with solids. Since their quantitative analysis typically has to take into account multiple scattering, we will not consider them further in this short overview, despite their undisputed usefulness.

Grazing incidence geometry for surface sensitivity

The single-scattering approximation for X-rays and neutrons is related to the weaker scattering cross section, so that the penetration depth for normal incidence is higher and 'surface sensitivity' is typically achieved with a specific trick, namely by employing 'grazing incidence', i.e. an angle of incidence α_i in the range of the angle of total reflection or below, i.e. $\alpha_i \sim 0.1^\circ$. The effective penetration depth of the 'evanescent wave' can then be as low as $\sim 10 \text{ \AA}$ (X-rays at gold surface).

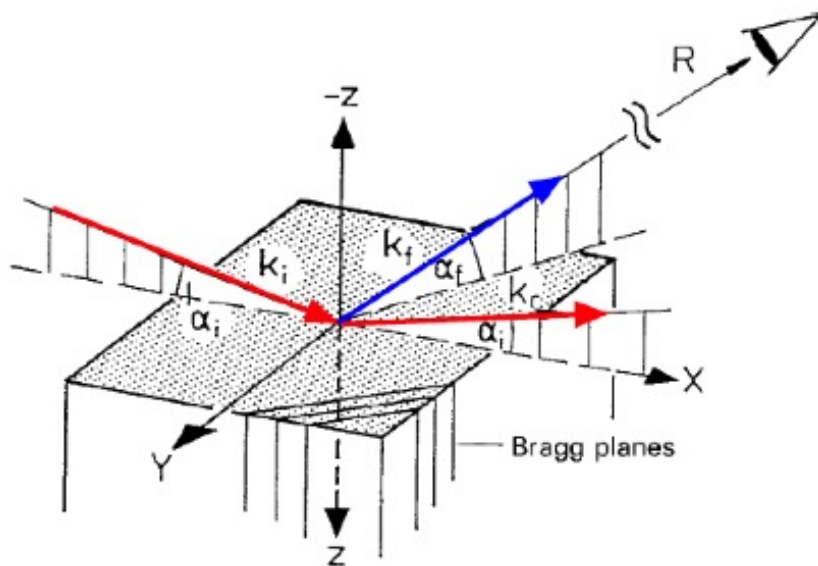


Fig. 7.3: Geometry of grazing-incidence X-ray diffraction (blue) and X-ray reflectometry (red)

Typical techniques and applications

The list of nanostructures, the structure of which has been solved, is virtually endless, not only in terms of the materials, but also in terms of the types and geometries, i.e. thin films, nanoparticles, quantum dots on a surface, multilayers, superlattices, etc.

We will not attempt to summarize all of these here, but rather refer to the selected examples provided in the Appendix (pdf of PowerPoint slides).

In brief, with a smart understanding of the concept of the Fourier transform, any nanostructure can be characterized, and obviously small length scales in real space (atomic

spacings) translate into small q 's in reciprocal space, whereas larger length scales in real space (size and shapes of nanoparticles, film thicknesses of several monolayers etc.) translate into small q 's in reciprocal space (and thus small scattering angles, so that 'small angle scattering', SAXS and SANS for X-rays and neutrons, respectively) is scattering from objects larger than atoms.

In addition, there are aspects of the scattering, which enter exclusively due to the symmetry break at the surface, i.e. due to the deviation from a bulk structure.

Keywords are:

- grazing-incidence X-ray diffraction (GIXD) (see above)
- reflectometry (X-rays or neutrons) from surfaces/interfaces/thin films
- crystal truncation rods (CTR's) from the surface of a bulk crystal

Also, for very thin samples experiments in transmission geometry are an option.

Furthermore, for mesoscopic nanostructures diffraction experiments with very small beams (around 100 nm in diameter, 'nanodiffraction') have become possible at synchrotron sources with suitable X-ray optics.

7.1.4 Scattering from a rough surface

When the surface of a film is absolutely flat, the X-rays (or neutrons) are reflected from it at the exit angle matching the incidence angle, $\alpha_f = \alpha_i$ (specular reflection). Therefore, if we illuminate a flat surface with a plane incident X-ray wave, there will be a single direction of the scattered wave. In other words, on the detector behind the sample (see Fig. 7.3 with the sketch of the setup), we will observe just a single bright spot corresponding to specular reflection.

However if the surface is not flat, the X-ray photons reflected from different parts of the surface will have different directions. The rougher is the surface, the broader will be the distribution of the scattered photons. This is the physical reason for observing so-called diffuse scattering - a non-zero scattered intensity around the specular reflection.

If the system of coordinates is chosen in such a way, that z-axis points perpendicular to the average surface and x-axis and y-axis are parallel to the average surface, the condition for a specular reflection would be an absence of the components of the scattering vector \mathbf{q} parallel to the xy-plane. In other words, specular reflection is characterized by $q_x = q_y = 0$ and diffuse scattering is observed for $q_x \neq 0$ or $q_y \neq 0$. The total scattered intensity can be written as

$$I(\mathbf{q}) = I(\mathbf{q})_{\text{spec}} + I(\mathbf{q})_{\text{diff}}, \quad (7.11)$$

$$I(\mathbf{q})_{\text{spec}} = \frac{r_e^2 \rho_e^2}{q_z^2} L_x L_y e^{-q_z^2 \sigma^2} (2\pi)^2 \delta(q_x) \delta(q_y), \quad (7.12)$$

$$I(\mathbf{q})_{\text{diff}} = \frac{r_e^2 \rho_e^2}{q_z^2} L_x L_y e^{-q_z^2 \sigma^2} \iint [e^{q_z^2 C(x,y)} - 1] e^{-iq_y y} e^{-iq_x x} dx dy. \quad (7.13)$$

Here $r_e \approx 2.8 \cdot 10^{-5}$ Å is classical radius of the electron, L_x, L_y are dimensions of the surface in xy-plane, $\sigma = \sqrt{\langle z^2 \rangle - \langle z \rangle^2}$ is root-mean-square (rms) roughness of the surface and $C(\Delta x, \Delta y) = \langle h(x + \Delta x, y + \Delta y) \cdot h(x, y) \rangle$ is the height-height correlation function. This means that X-ray scattering can access not only the rms roughness of the surface, but also the correlation function of the surface. This allows one to extract, for example, average size of a mound on the rough surface. The averaging in this case is performed over the size of an X-ray beam footprint (which is typically between 100 microns to centimeters). Therefore, characterization of the surface roughness via grazing-incidence scattering is *statistically* much more reliable and efficient than, for example, various microscopy techniques (i.e. AFM).

More information about the correlation functions is given in the following section.

7.1.5 Statistical description of surfaces by correlation functions

We consider a film on a substrate or an A-on-A depositon (homoepitaxy; see later section for definition) of some thickness well beyond the monolayer. The surface profile, i.e. the height h as a function of lateral coordinate (x, y) is described by $h(x, y)$.

The surface width, i.e. the root-mean-squared roughness

$$\sigma = \langle [h(x', y') - h(x, y)]^2 \rangle_{((x'-x), (y'-y) \rightarrow \infty)}^{1/2} \quad (7.14)$$

where $\langle \dots \rangle$ means the average over all lateral positions, will then have some significant value typically well above a monolayer thickness.

If we want to compare this to theoretical predictions or to other surfaces, it is obviously not practical to compare the complete function $h(x, y)$, but to extract certain features which are *statistically significant*.

How do we describe the surface appropriately in a statistically significant way? A typical approach is the height difference correlation function

$$G(r) = \langle [h(x + r) - h(x)]^2 \rangle \quad (7.15)$$

which is related to the height-height correlation function

$$C(r) = \langle [h(x + r)h(x)] \rangle \quad (7.16)$$

by

$$G(r) = 2\sigma^2 - 2C(r) \quad (7.17)$$

Typical examples are illustrated next.

(see also correlation function in the condensed matter lecture in the fifth term)

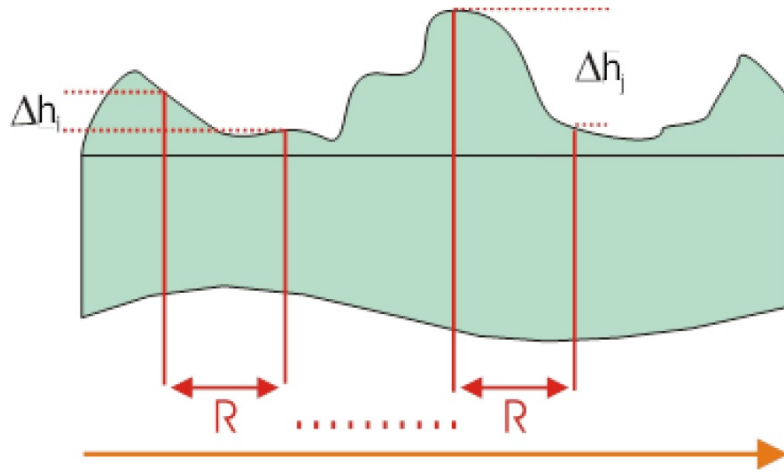


Fig. 7.4: Schematic of a rough surface for the calculation of the height-height correlation function

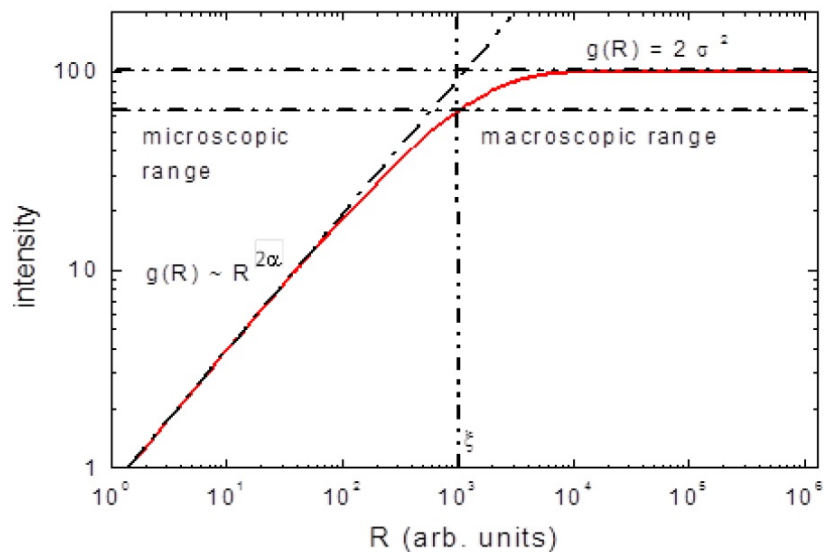


Fig. 7.5: Shows the typical shape of the correlation function, which can be intuitively interpreted (see also Pimpinelli/Villain, p.207).

Initially, the height difference is small, since the probability to experience a significant height difference relative to the starting point for small lateral distances r is small.

At some lateral distance ξ typically the correlations are 'lost', but the differences also do not increase anymore and the 'maximum peak to valley height difference is reached'. Beyond ξ , the correlation function levels off to a constant value, which corresponds to $2\sigma^2$.

This type of correlation function is thus described by three parameters

- 1) Initial slope, given by the 'Hurst exponent (parameter)', usually called h or α .
- 2) Lateral correlation length, ξ .
- 3) Value of the correlation function for infinite lateral distances, i.e. roughness, σ .

In order to connect the small r and the large r limit, often an approximate form of $C(r)$ is used, namely

$$C(r) = \sigma^2 \exp[(-r/\xi)^2] \quad (7.18)$$

Below we discuss typical examples for $G(r)$ or $2C(r)$.

Scaling arguments (why the initial slope follows a power law etc.) are given later.

Examples (for constant roughness in all cases)

Note that the figures (courtesy of Universität Kiel) show $C(r)$ instead of $G(r)$, but this essentially only inverts the sign.

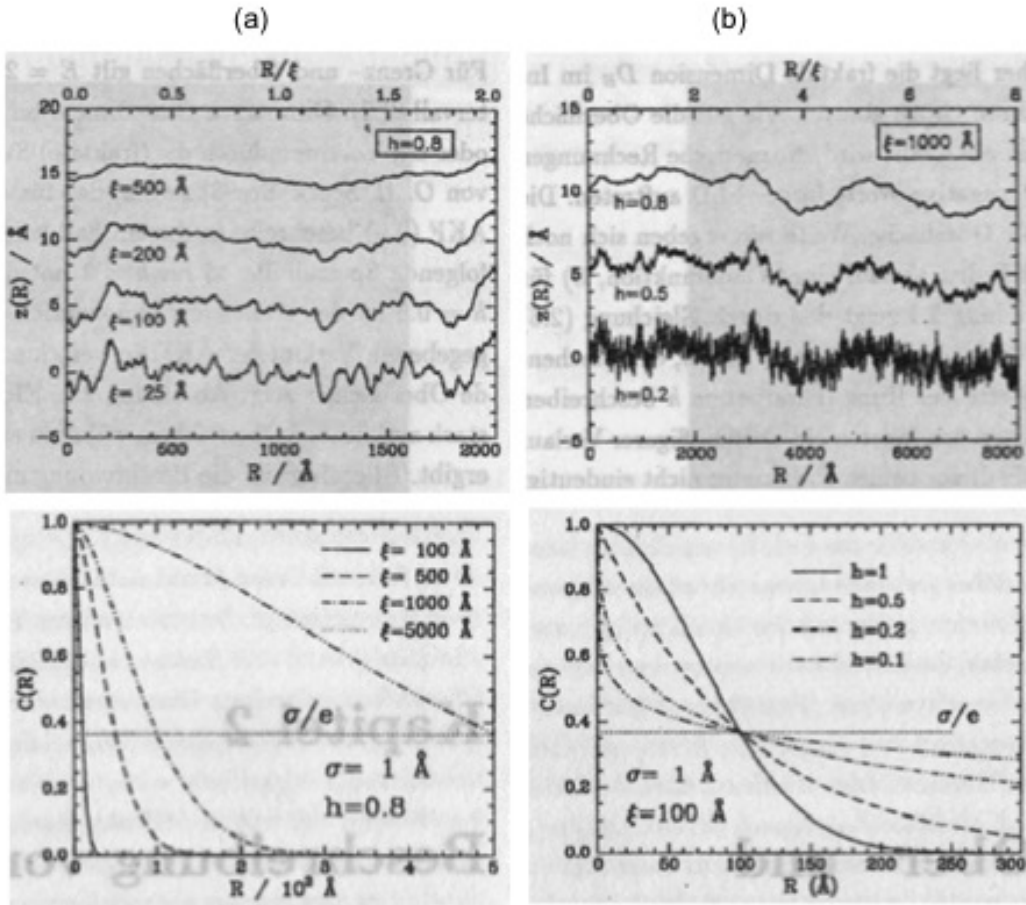


Fig. 7.6: Variation of the (a) correlation length ξ ; (b) Hurst parameter; and corresponding correlation functions

7.1.6 Notes on the background of scaling laws in growth physics and self-affinity

Pimpinelli / Villain, p.208 (good explanation even with calculation for example)
 Michely / Krug, p. 197 (we follow their introduction here)

The concepts of fractal geometry have been used extensively to characterize structures formed in growth far from equilibrium. For our purposes, fractals can be defined as objects that show statistical scale invariance, which means that they look the same (in a statistical sense, i.e. exhibit the same parameters characterizing their morphology) under arbitrary levels of magnification (i.e. in images of any scale).

This self-affinity is then expressed in a transformation

$$h(x) \longrightarrow b^{-\alpha} h(bx) \quad (7.19)$$

where b is a scale factor and the exponent α the Hurst parameter ($\alpha = 1$ for self-similarity and $\alpha < 1$ for self-affinity).

This has implications for the height difference correlation function, namely

$$G(r) = b^{-2\alpha} G(br) \quad (7.20)$$

Setting $b = 1/r$ directly leads to

$$G(r) \sim r^{2\alpha} \quad (7.21)$$

which is the hallmark of self-affine scaling. This is indeed found in many systems in a good approximation for small lateral distances r . This also implies further scaling laws (here without proof; see Michely/Krug, p.199)

$$\sigma(t) \sim t^{\alpha/z} \quad (7.22)$$

$$\xi(t) \sim t^{1/z} \quad (7.23)$$

We note that more generally than the above presentation one writes

$$\sigma(t) \sim t^\beta \quad (7.24)$$

where

$$\beta = \alpha/z + \lambda \quad (7.25)$$

$\lambda = 0$ corresponds to the 'no steepening' case.

$\lambda > 0$ is referred to a *anomalous*

In other words, the equation on the previous page corresponds to the no steepening case.

The typical values for these exponents are 'of the order of 1', but of course depend on the specific model, i.e. mechanism of growth, which applies to a given system. In practice, the exponents are determined experimentally and then compared to different models.

7.2 Microscopy

A central element in the development of nanotechnology is the constant improvement of already existing measurement techniques and the introduction of new methods and techniques in order to characterize surfaces (e.g. topography, adsorbates, crystal structure, electronic and magnetic properties) and lateral nanostructures *in real space* down to the atomic scale.

Main microscopy techniques:

- Electron microscopy
 - Scanning electron microscopy (SEM) → absorption/excitation & reflection
 - Transmission electron microscopy (TEM); often in combination with electron energy loss spectroscopy (EELS); also 'scanning'-mode (STEM)
- (Helium-)ion microscopy (new technique, introduction to the market 2011)
- Scanning probe microscopy (SPM)

7.2.1 Light microscopy

Light microscopy is a simple and flexible method to analyze samples with visible light in transmission or reflection.

Light microscopy is, however, fundamentally **diffraction limited**. Point-like light sources create an **Airy disc** in the image plane with a diameter of $d_{\text{Airy}} \simeq 1,22 \frac{\lambda}{n \sin(\alpha)}$, with the wavelength of the light λ , the refractive index of the medium in front of the objective n , the half-opening angle of the objective α and the numerical aperture $NA = n \sin(\alpha)$ (see Fig. 7.7(a)).

The **Rayleigh criterion** determines the resolution limit, where two spots can just be discerned from each other, to $d \simeq 0,61 \frac{\lambda}{NA}$. At this distance the maximum of the Airy-disc coincides with the first minimum of the second Airy-disc, see Fig. 7.7(b). According to Ernst Abbé it is therefore only possible to resolve structures down to a minimum distance of about 200 nm.

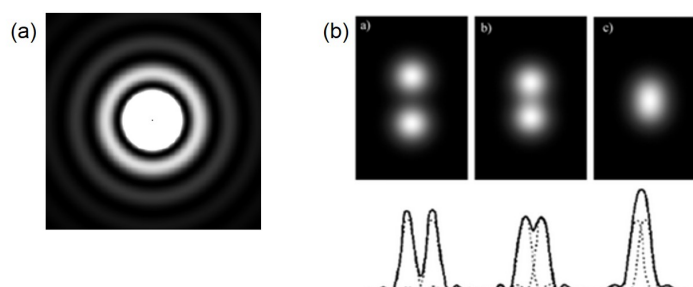


Fig. 7.7: (a) Diffraction image of a point source: Airy disc, (b) illustration of the resolution limit (panel (b)-b))

Conventional light microscopy is therefore **not** suitable for the imaging of nanostructures; only special new developments make it possible to image with light beyond the diffraction limit.

Note that due to the pioneering work by Eric Betzig, Stefan Hell, and William E. Moerner (Nobel Prize in Chemistry 2014) the Abbé resolution limit of optical microscopy has been overcome by ideas related to essentially nonlinear response. Considering fluorescence microscopy, the key ingredient is to deexcite ("silence") the fluorescing molecules in an area *around* the area of interest (which is then supposed to be smaller than the limit of some 200 nm) by donut-shaped illumination. The response to this is non-linear, and only the small spot in the center of the donut can exhibit fluorescence, which is then well below the conventional diffraction limit.

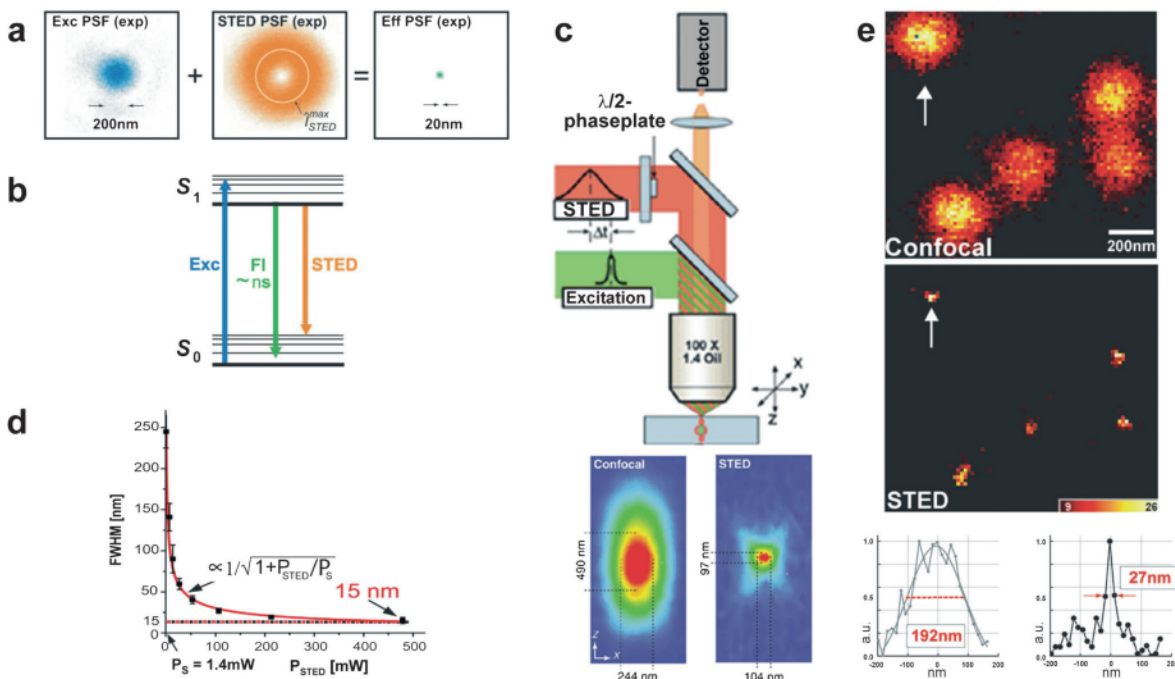


Fig. 7.8: The principles of STED (STimulated Emission Depletion) microscopy. a) Measured profiles of excitation beam (left), STED beam (center) and effective PSF (right). b) A Jablonski diagram showing the basic transitions occurring in STED microscopy. Fluorophores are excited to the S_1 state using the excitation laser. The STED laser deexcites molecules outside the center of the PSF from the ground vibrational state of the excited state to a high vibrational state of the ground state. The emitted light is blocked at the detector with proper filters. Molecules at the center of the PSF return to the ground state via fluorescence and are detected with an effectively reduced PSF. c) Upper: the first realized STED microscope. Lower: the PSF from 48 nm beads labeled with the fluorophore LDS 751 measured using confocal microscopy and with STED microscopy. In the STED image, the lateral size of the PSF was reduced from 490 nm to 97 nm. d) The full-width half-maximum (FWHM) of effective PSF as a function of STED beam power. e) Synaptotagmin I molecules within endosomes. The confocal image (top) shows diffraction limited spots with a size around 200 nm. The STED microscope image (center) reveals the true size of the spots to be around 30 nm. (after Möckl et al., Angew. Chem. Int. Ed. **53**, 13972 (2014))

Until the beginning of the 20th century, light microscopy was the only available microscopy technique. Only in the 1930s Ernst Ruska opened up new possibilities for high-resolution imaging with the development of electron microscopy. This was followed by the development of scanning probe microscopy by Gerd Binnig and Heinrich Rohrer starting from the 1980s (Nobel prize for Ruska, Binnig and Rohrer 1986).

7.2.2 Electron microscopy

a) Electron optics

Electron sources: electrons are emitted by heating and/or field emission from a filament (tungsten) in vacuum, see sketch in Fig. 7.9. In Fig. 7.10 the work function is shown schematically for the three cases of thermal or thermionic emission, Schottky emission or field emission. In case of thermal emission the full energy of the work function of the electrons from the metal up to the vacuum level has to be provided by heating. By application of a strong electric field to the tip, the barrier height is reduced.

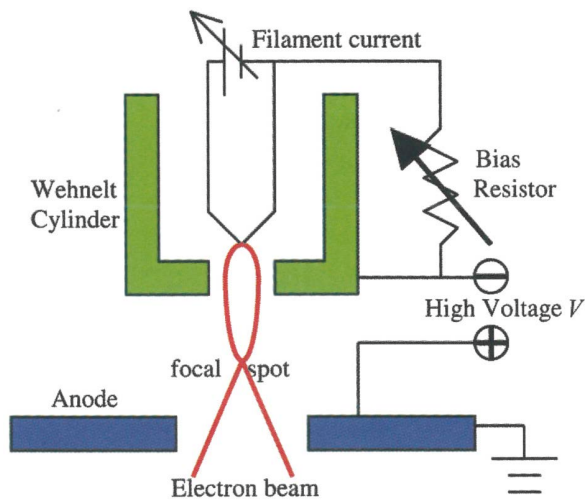


Fig. 7.9: Principle of an electron source: The beam is created by thermal emission from the filament and focussed by the (negatively charged) Wehnelt cylinder. The high voltage V accelerates the electrons. In the case of a field emission gun the filament is replaced by a tip with radius $< 1 \mu\text{m}$ [R. Waser (Ed.), Advanced Electronic Materials and Novel Devices, Wiley-VCH (2003)].

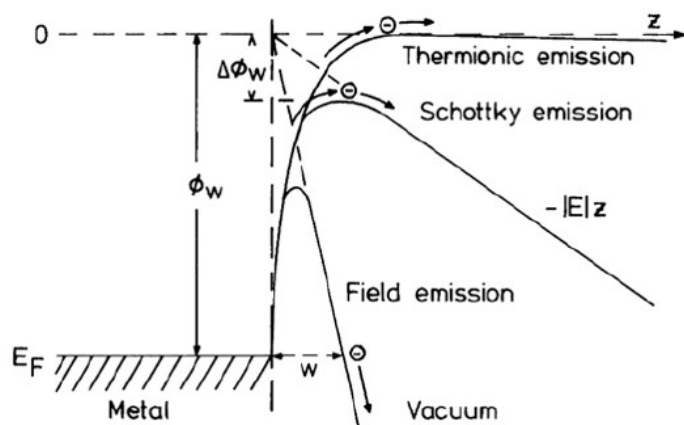


Fig. 7.10: Energy diagram for electron emission from thermal, Schottky and field emitters

Important parameters for electron sources:

- size (and shape) of the source → determine the resolution
- intensity of the beam (*brightness* in A/cm²/sr)
- energy distribution (*spread*) → causes chromatic aberration of the lenses

Common types of sources:

- thermionic emission filament (W): out-dated; least vacuum requirements
- thermionic emission tip: LaB₆-monocrystal (tip radius $r_s \sim 5 \mu\text{m}$)
- Schottky-emitter: ZrO-coated tip, reduces work function ($r_s < 0.5 \mu\text{m}$)
- field-emitter: 'cold emission', work function reduced by electric field ($r_s \ll 0.5 \mu\text{m}$), highest requirements for vacuum

Source type	brightness [A/cm ² /sr]	source size [μm]	energy spread [eV]	Operating vacuum [mbar]	operating temperature [K]	life time [h]
tungsten filament	10^5	25	2..3	10^{-6}	2700	100
LaB ₆ tip	10^6	10	2..3	10^{-8}	1700	500
Schottky emitter	10^8	0.02	1.0	10^{-9}	1800	> 1000
cold field emitter	10^9	0.005	0.2	10^{-10}	300	> 1000

Fig. 7.11: Typical parameters for electron guns [R. Waser (Ed.), Advanced Electronic Materials and Novel Devices, Wiley-VCH (2003); Kap.11].

The electron beam is focussed by **electron-optical components**, i.e. by electromagnetic (condenser-, objective-, projector-) lenses and apertures, and scanned across the sample surface line by line by deflector coils. The focal lengths of the lenses are tunable via the respective currents.

The nominal **resolution** can be expressed based on the wavelength λ , analogous to the resolution limit A in optical microscopy. From

$$A \approx \frac{\lambda}{n \sin \alpha} \quad (7.26)$$

where $n \sin \alpha$ is the numerical aperture (refractive index n ; collimation-/divergence-angle α), together with the de Broglie-wavelength λ_{dB} of the electrons

$$\lambda_{dB} = \frac{h}{\sqrt{2m_e E_0}} = \frac{h}{\sqrt{2m_e eV}} \quad , \quad (7.27)$$

with Planck's constant h , the electron mass m_e and the kinetic energy of the electrons $E_0 = eV$ (e : elementary charge; V : acceleration voltage) there follows a diffraction-limited resolution $\propto 1/\sqrt{V}$.

Example: With $V = 100 \text{ kV} \rightarrow \lambda_{dB} \approx 0.04 \text{ \AA} = 4 \text{ pm}$

This (sub-atomic) resolution however cannot be reached due to lens errors. Nevertheless, TEM achieves a spatial resolution in the sub-Å regime! A new generation of aberration-corrected systems was introduced to the market some years ago.

b) Scanning electron microscopy (SEM)

SEM works in reflection mode. The incoming electron beam scans over the surface. By scattering and interaction with the material, in each point secondary electrons are produced as well as further elastically and inelastically scattered electrons, and possibly X-rays. The corresponding **interaction volume** for the different processes is shown in Fig. 7.12(a). The individual signals can be detected with different detectors in backscattering.

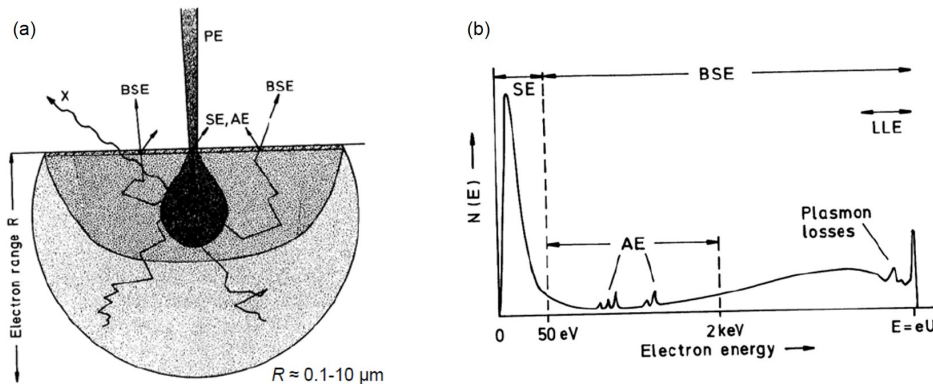


Fig. 7.12: (a) Interaction volume for different interactions of a focussed electron beam with the sample surface; PE: primary electrons, SE: secondary electrons, BSE: backscattered electrons, AE: Auger electrons, X: X-rays; (b) electron spectrum.

Interaction processes:

- Elastic backscattering:
backscattered primary electrons (PE) with primary energy E_0
- Inelastic backscattering:
backscattered electrons, which due to (typically plasmonic) excitations in the solid are emitted with an energy loss of about $\approx 50 \text{ eV} \rightarrow$ specific for each material (depending on the band structure, crystal structure, interfaces and defects)
- Characteristic X-rays:
Primary electrons ionize atoms by removing electrons from inner shells, \rightarrow transition of an electron from a higher shell emits X-rays with a characteristic energy, \rightarrow material specific line spectrum, detection by energy dispersive X-ray-analysis (EDX)
- Auger-electrons (AE):
Alternatively to emitting an X-ray photon, it is also possible that an Auger electron from an outer shell is emitted, \rightarrow strongly dependent on the element (100 eV - 1 keV)
- Secondary electrons (SE):
excited electrons which leave the surface after multiple scattering,
 \rightarrow broad energy distribution with a maximum $< 50 \text{ eV}$

SEM parameters:

- typical beam energies: $E_0 = 0.5 - 30 \text{ keV}$
- diameter of the focus on the surface sample & typical resolution: $\sim 1 - 5 \text{ nm}$

The range of charged particles with (primary) energy E_0 in a solid of density ρ is approximately given by

$$R_p(\text{nm}) \simeq \frac{\kappa [E_0(\text{keV})]^p}{\rho(\text{g/cm}^3)} . \quad (7.28)$$

The parameters κ and p for electrons are given within the Kanaya-Okayama-model: $\kappa \approx 70 - 100$; $p \approx 1.4 - 1.8$. The range of primary electrons (size of the interaction volume) for $E_0 \simeq 10 \text{ keV}$ is therefore within the range of μm .

Signals arise from different processes during the interaction of the beam with the sample surface. This results in spatially resolved information on the surface properties by mapping the (integrally measured) detector signal to the beam position. By using different detectors (sensitive to electrons of different energies or to photons), different material properties and/or the topography can be imaged. The spatial resolution (lateral and information depth) strongly depends on the detected signal (e.g. relatively poor for EDX, since X-rays emerge from the whole interaction volume; strongly surface sensitive for AE; SE due to their low mean free path within the material R_{SE} predominantly originate from the area of the beam spot on the surface).

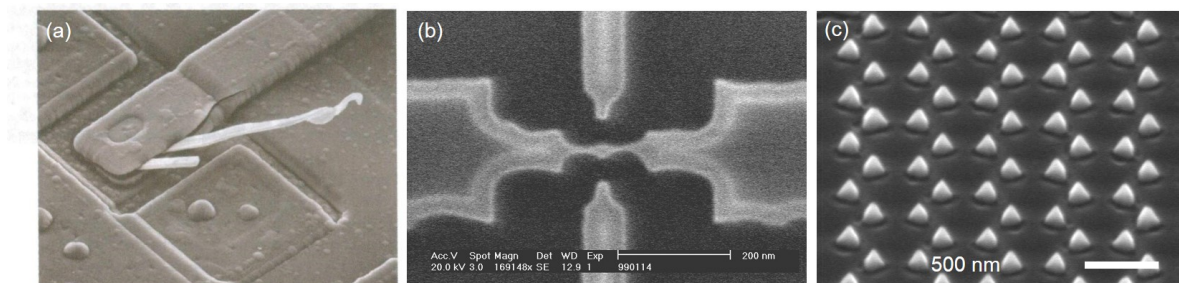


Fig. 7.13: SEM images: (a) defective semiconductor device; (b) quantum dot; (c) gold nano cones fabricated by nanosphere lithography [R. Waser (Ed.), Wiley-VCH, Weinheim (2003), Kap.11; AGs Kern/Wharam/Fleischer, Universität Tübingen].

Contrast mechanisms:

The contrast is a function of the number of electrons/photons that reach the detector. In order to interpret the recorded images, it is essential to take into account the interaction of the electron beam with the surface. This interaction yields the corresponding contrast, since the escape probability depends sensitively on different surface properties. The information is encoded in grey scale images.

- Strong *edge contrast* in the detection of secondary electrons (SE)
- *Shadow contrast* due to the position of the SE detector with respect to the sample
- *Material contrast* especially for inelastically backscattered electrons and AE
- *Potential contrast* especially for the detection of low-energy electrons
- *Roughness contrast* due to the higher escape probability for rough surfaces
- *Crystal-orientation contrast*, detectable by **electron backscatter diffraction (EBSD)**, where a diffraction image of the BSE is recorded
- *Magnetic contrast*, etc.

c) Transmission electron microscopy (TEM)

Beam path:

In TEM, the electron beam passes through the sample, which has to be transparent for the electrons. The electrons are transmitted through the very thin sample and detected subsequently.

A condenser lens system (only one lens as shown in Fig. 7.14) defines the electron beam. Collimation is achieved by an objective lens and an aperture (analogous to light microscopy). This way, the number of diffraction spots that contribute to the image is restricted. The 'sector' lens enlarges the (diffraction) image. The projection lens images the electrons on the screen or camera.

There are two possible modes of operation:

- i) microscopic imaging mode, → arrangement of the atoms [Fig. 7.14(a)]
- ii) diffraction mode, → crystal analysis [Fig. 7.14(b) and Fig. 7.15]

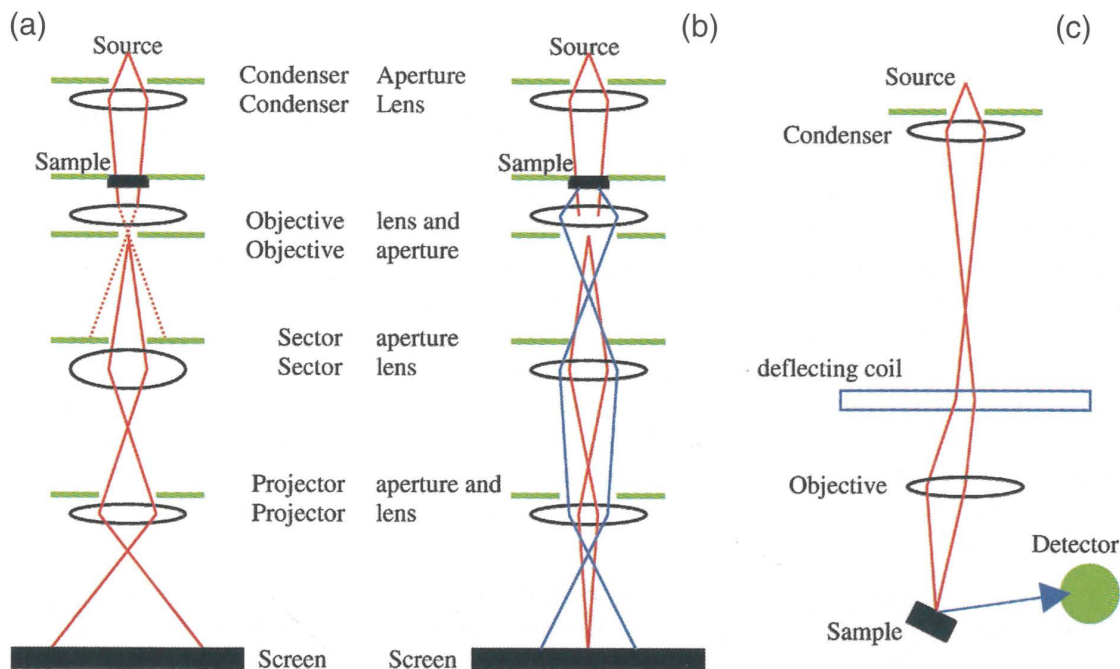


Fig. 7.14: Beam paths in TEM and SEM. (a) TEM imaging mode, (b) TEM diffraction mode: blue lines = Bragg reflexes of the lattice, red lines = as in (a). (c) SEM imaging [R. Waser (Ed.), Advanced Electronic Materials and Novel Devices, Wiley-VCH, Weinheim (2003); Kap.11].

Sample preparation:

TEM samples have to be very thin, such that the electrons can pass through them. For this purpose, an elaborate sample preparation is required, with thinning by ion beam etching and/or mechanical polishing (TEM is a destructive method), which can produce artefacts.

For non-ultrahigh-resolution images it is sufficient to thin the sample to ~ 100 nm; for atomic resolution, the sample thickness needs to be $\lesssim 10$ nm.

Examples:

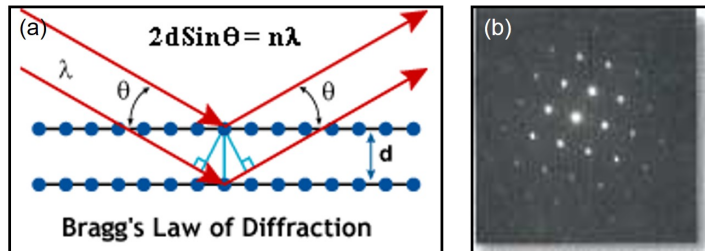


Fig. 7.15: (a) Schematic representation of Bragg diffraction at a crystal lattice, (b) resulting Bragg reflexes for different crystallographic directions in TEM diffraction mode [Presentation by M. Meyyappan, NASA Ames Research Center].

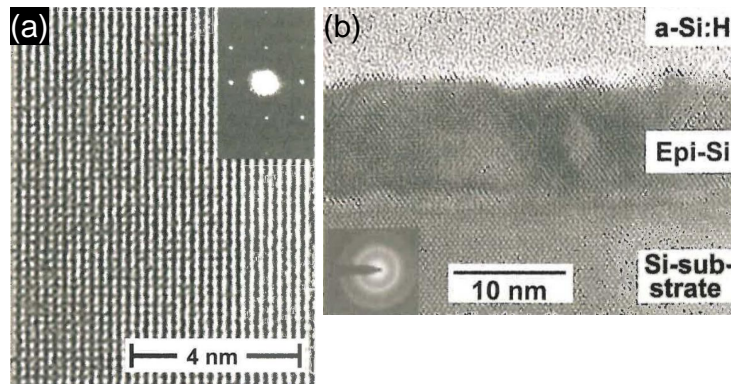


Fig. 7.16: (a) high-resolution TEM image of a Au single crystal where the crystallographic planes are clearly visible; Inset: diffraction image with Bragg reflexes around the undiffracted beam. (b) Cross-section TEM image of an amorphous Si-layer on crystalline Si. Inset: diffraction image (only small-angle regime, such that the Bragg reflexes of the substrate are not visible). The ring-like pattern is typical for amorphous samples [R. Waser (Ed.), Advanced Electronic Materials and Novel Devices, Wiley-VCH, Weinheim (2003); Kap.11].

7.2.3 Ion microscopy

The setup for ion microscopy is highly analogous to SEM, see Fig. 7.19. Here, too, a focussed beam of charged particles is produced, with which the surface is scanned line-by-line.

Due to the higher mass m of ions compared to electrons (for He: factor of 7300), the theoretical diffraction-limited resolution is improved. The de-Broglie-wavelength $\lambda_{dB} \propto 1/\sqrt{m}$ is clearly in the sub-atomic range and decreases with increasing mass of the ions, see Fig. 7.20.

However, with increasing ion mass also the damage to the surface increases, → see focussed ion beam etching in Sec. 3.2.4. For this reason Ga^+ ion beams are mainly used for milling instead of imaging. While a stable gallium ion beam can be produced from a *liquid metal ion source* (LiMIS, see Sec. 3.2.4), for other ions other sources are required.

An important development of the past years was a stable, nearly point-like helium ion source with a high intensity ($> 10^9 \text{ A/cm}^2/\text{sr}$).

The *gaseous field ion source* (GFIS, see Fig. 7.21) consists of a tip which is cooled

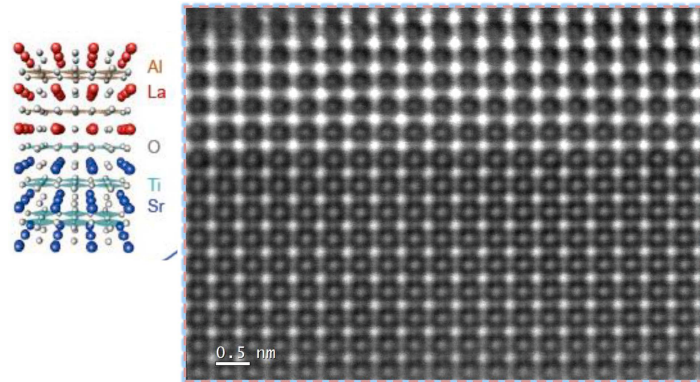


Fig. 7.17: (a) High-resolution TEM image of the interface between a SrTiO₃ substrate and a LaAlO₃ film, which was epitaxially grown by *pulsed laser deposition* (PLD), with an almost perfect interface [Fabio Miletto Granozio, CNRS-SPIN, Napoli].

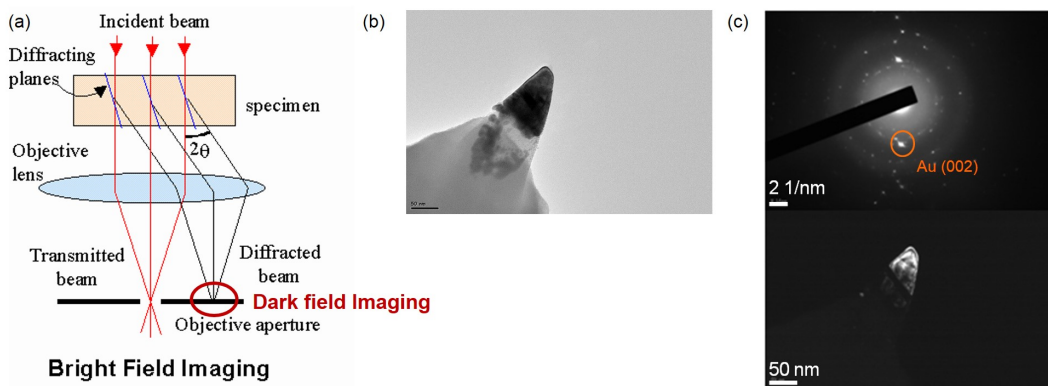


Fig. 7.18: (a) Schematic of bright-field imaging vs. dark-field imaging (1^{st} diffraction order) in TEM; (b) bright-field TEM image of a gold nano-cone on a cantilever tip; (c) top: diffraction image, from which the dominant Au(002)-Bragg reflex is selected; bottom: reconstructed dark-field image from the signal of the Au(002) reflex, where only the part of the nano-cone with crystal orientation Au(002) is highlighted. [M. Fleischer et al., ACS Nano 5, 2570 (2011)].

to about 70 K in a helium gas ($\sim 10^{-6}$ mbar). By applying a strong electrical field, a pyramidal tip with a stable trimer at the apex is shaped. One of these three atoms is selected by an aperture in order to ionize the surrounding helium. The ionized He atoms are accelerated towards the sample. For this reason, the beam source has an effective diameter of only ~ 0.3 nm (development by Bill Ward, *Atomic Level Imaging Systems* (ALIS) Corp., Peabody (USA); belongs to Carl Zeiss SMT since 2007).

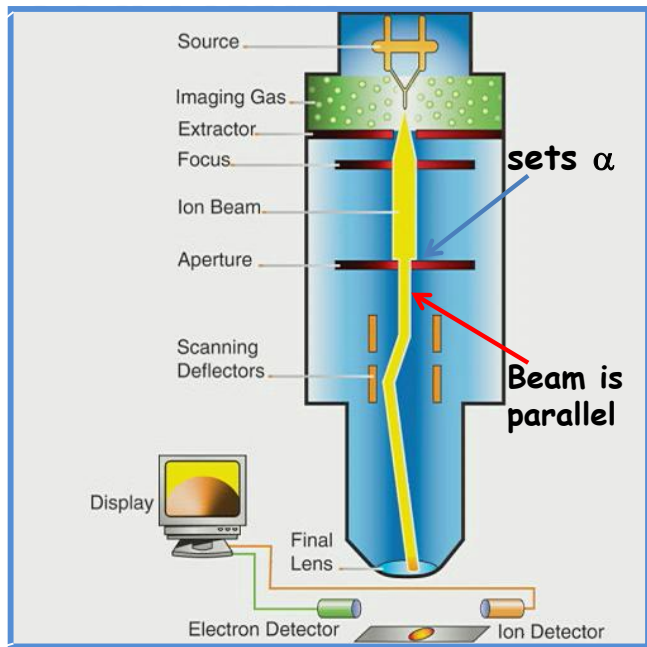


Fig. 7.19: Schematic representation of the configuration of a helium ion microscope [from D.C. Joy, Springer (2013)].

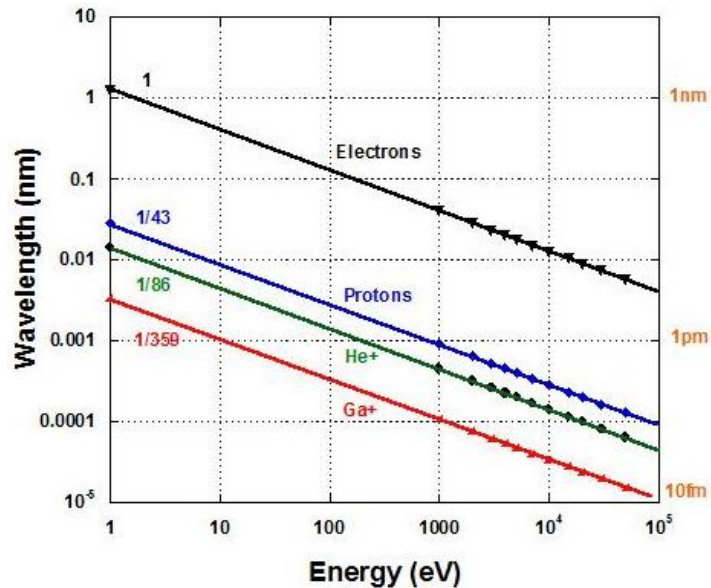


Fig. 7.20: Comparison of the de Broglie wavelengths of electrons and various ions as a function of energy [D.C. Joy, *Helium Ion Microscopy – Principles and Applications*, Springer (2013)].

Advantages of the HeIM with respect to SEM:

- extremely small effective diameter of the ion source $\sim 3 \text{ \AA}$ and 'spot'-diameter on the sample surface $\sim 5 \text{ \AA}$, \rightarrow sub-nm resolution
- more narrow, more strongly oriented interaction volume (fig. 7.22)
- lower range of He^+ at same E_0 , \rightarrow high surface sensitivity
- small wavelength \rightarrow resolution not limited by diffraction limit, very small collimation angle α possible, \Rightarrow significantly higher depth of field ($> 1.5 \mu\text{m}$)
- strong contrast (high SE yield); strong material contrast in backscattered ion image, \rightarrow intensity $\propto Z^2$ (Z : atomic number)
- *channeling* effect of the He ions, \rightarrow information on crystal orientation
- less charging effects for imaging of insulating samples

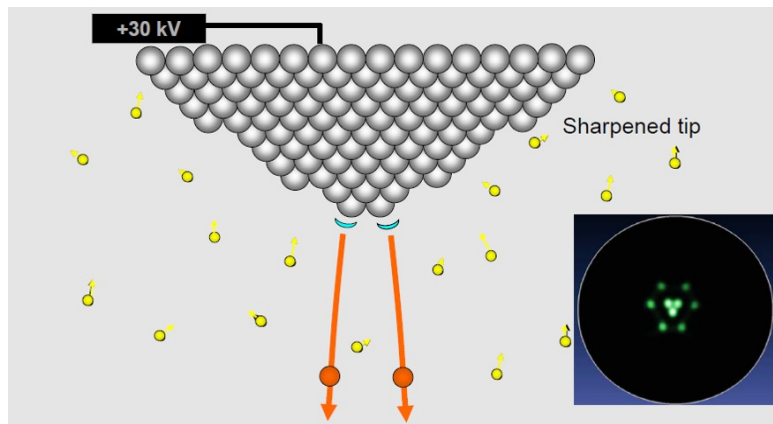


Fig. 7.21: GFIS: Principle of field ionization at the tip; inset: Image of the trimer at the tip apex [<http://www.zeiss.de>].

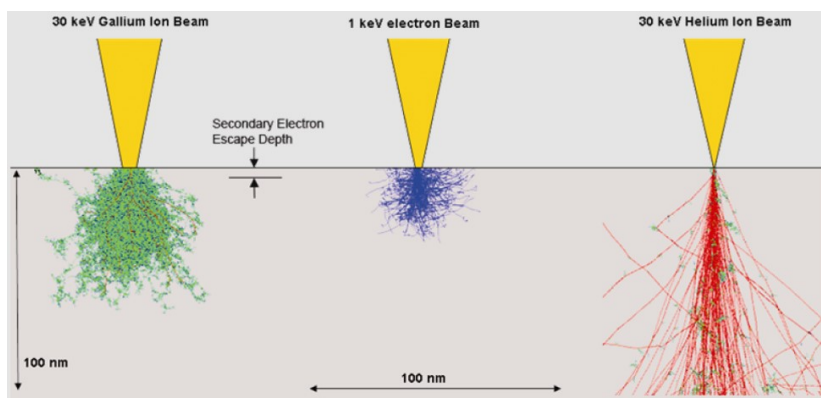


Fig. 7.22: Comparison of the interaction volume of a Ga-ion beam, electron beam and He-ion beam [P. Gnauck, Carl Zeiss NTS; Southampton Nanofabrication Center].

7.2.4 Scanning probe microscopy

SPM = *Scanning Probe Microscopy*

Scanning probe microscopy methods are being developed since the 1980s. They are among the most important techniques for the characterization of surfaces in real space. The first development was the *Scanning Tunnelling Microscope* invented in 1981 by Gerd Binnig and Heinrich Rohrer (IBM Rüschlikon, nobel prize in physics 1986 with E. Ruska).

Imaging principle:

The common principle of the characterization of the surface is based on the interaction between a sharp tip that is scanned across the sample with the surface, see Fig. 7.24.

Depending on the **interaction**, different techniques are distinguished:

- van-der-Waals Force (*atomic force microscopy*, AFM)
- tunnelling current (*scanning tunnelling microscopy*, STM)
- magnetic force (*magnetic force microscopy*, MFM)
- electrostatic force (*electrostatic force microscopy*, EFM)
- light (*scanning near-field optical microscopy*, SNOM)

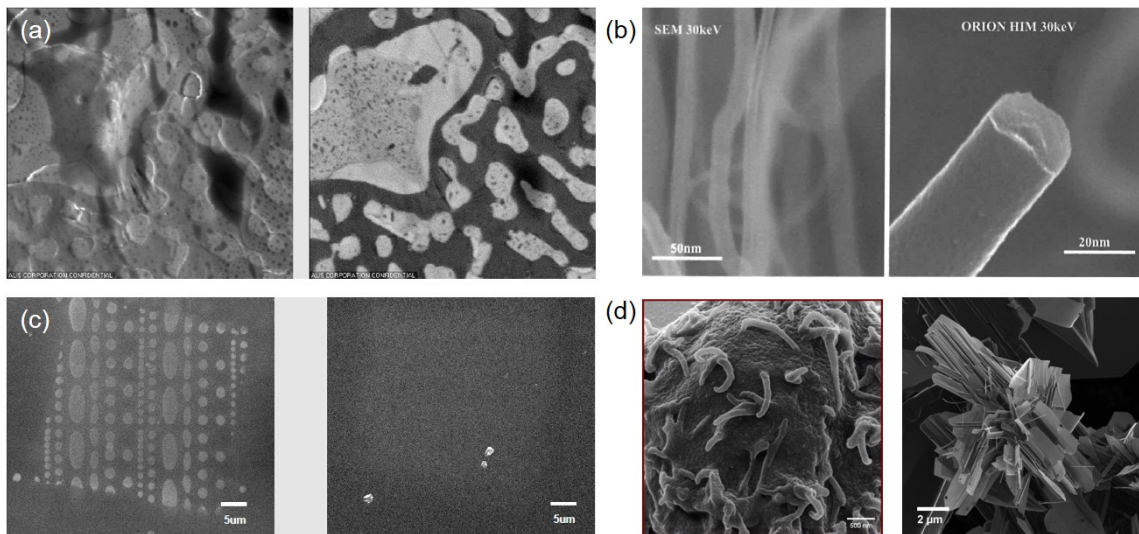


Fig. 7.23: (a) Material contrast Au on AuC and (b) carbon nanotubes (left SEM, right HIM); (c) NBPT-monolayer on gold (left HIM, right SEM); (d) white blood cells and hydroxyapatite-crystal with high depth of field in HIM [(a,c,d) Carl Zeiss NTS; (b) D.C. Joy, Springer (2013); (d) B. Ward et al., Photonics Spectra, 08/2007].

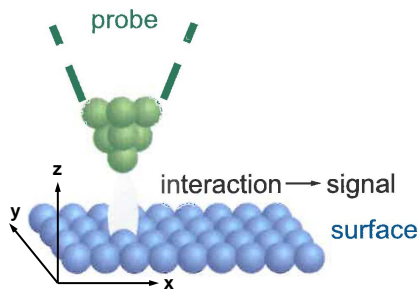


Fig. 7.24: Principle of scanning probe microscopy [R. Waser (Ed.), Advanced Electronic Materials and Novel Devices, Wiley-VCH, Weinheim (2003); chap. 12].

- temperature (*scanning thermal microscopy*)
- acoustic properties (*scanning acoustical microscopy*)
- conductivity, capacity, elasticity, ...

Through the various interactions, information on electronic, topographic, optical, magnetic, mechanical, ... properties of the surface down to atomic resolution is gained.

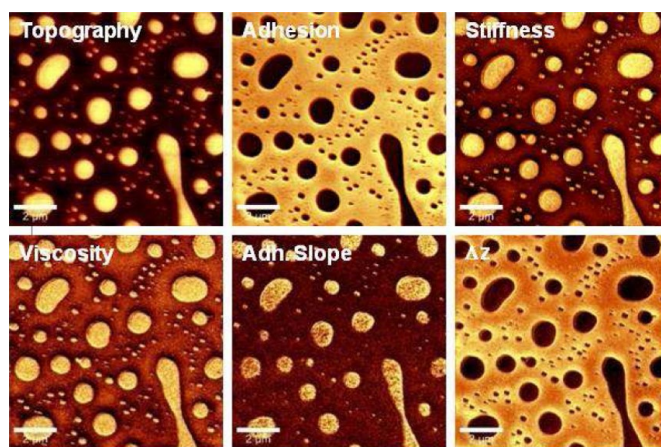


Fig. 7.25: Images of different properties of the same surface obtained by different scanning probe microscopy techniques [Witec-Webinar, <http://www.witec.de>].

a) Scanning tunnelling microscopy (STM)

STM has the highest spatial resolution of all SPM techniques.
Atomic resolution can be reached routinely.

STM requires electrically conducting surfaces (semiconductors, metals, superconductors) and tips (usually gold). STM is performed in UHV. The electronic surface properties are imaged.

Principle:

- sharp metallic tip = tunnelling tip as a probe
- application of a voltage V between tip and surface
- approach of the tip to the surface ($\leq 1 \text{ nm}$) \Rightarrow tunnel current I
- scanning of the tip with a piezo element (controlled via piezo voltages):
 \rightarrow scan areas of $\sim \text{nm}$ to $\sim \mu\text{m}$ with (sub-)nm increments, \Rightarrow image $I(x, y)$

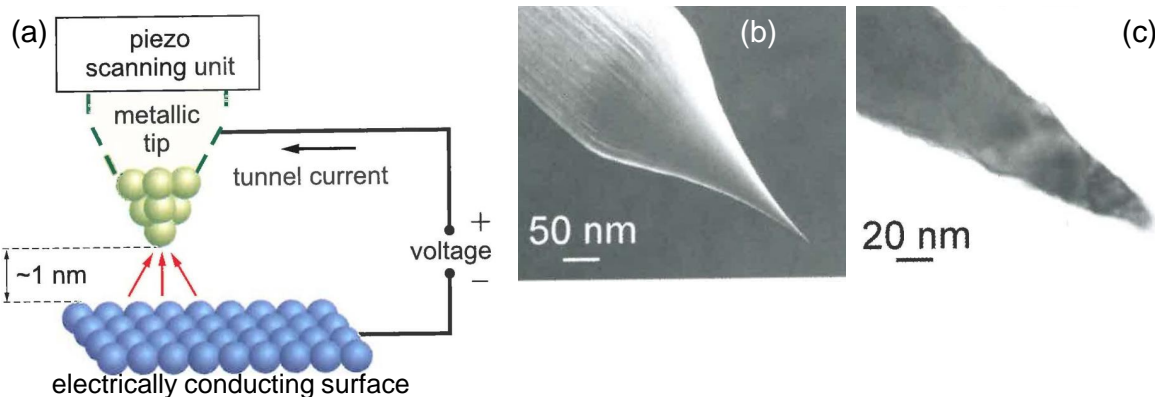


Fig. 7.26: (a) Schematic representation of STM: tunnel current as the measured signal; (b) SEM image and (c) TEM image of a typical metallic STM tip [R. Waser (Ed.), Advanced Electronic Materials and Novel Devices, Wiley-VCH (2003); chap.12].

Tunnelling effect:

Due to the tunnelling effect, transport of electrons through the vacuum ($\hat{=}$ potential barrier) between tip and surface takes place, see energy diagram in Fig. 7.27.

This quantum-mechanical effect occurs due to an overlap of the wave functions of the electronical states within the barrier (in the classically forbidden area).

The tunnelling probability decreases exponentially with the distance (tip to surface) and the height of the potential barrier (with respect to the energy of the tunnelling electron):

$$I \propto e^{-2\kappa z} , \quad (7.29)$$

where I is the tunnel current, κ a decay constant and z the tip-sample-distance. This exponential decrease is crucial for the high sensitivity of the measuring method, i.e., even minute changes of z are causing strong changes in the tunnel current. The direction of the tunnel current is determined by the polarity of the applied voltage V .

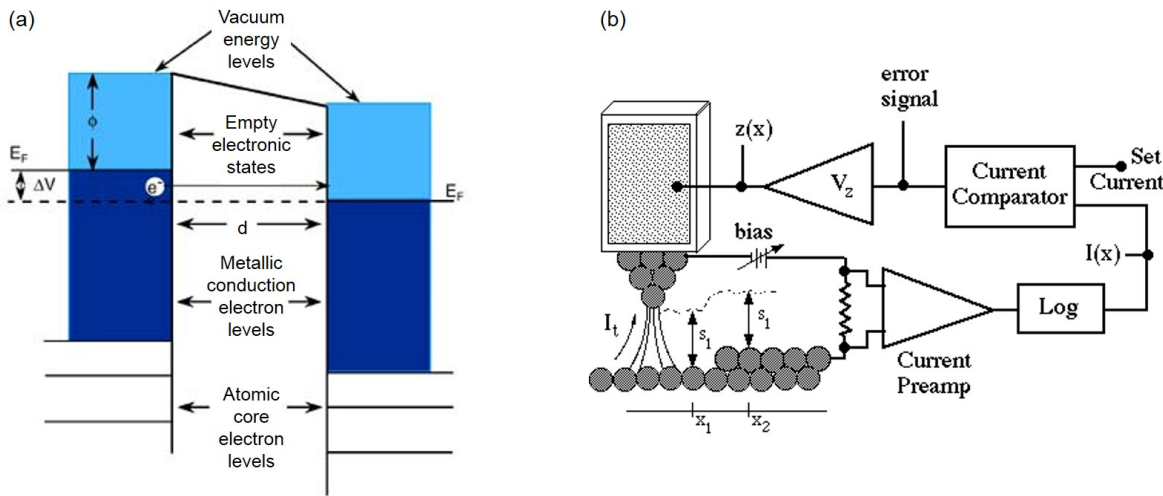


Fig. 7.27: (a) Energy diagram for the tunnelling process from surface to tip; (b) STM setup [http://www.mpi-halle.mpg.de; http://spm.aif.ncsu.edu].

The theoretical description dates back to J. Bardeen [Phys. Rev. Lett. 6, 57 (1961)], who described the weak overlap of the wave functions by a transfer Hamiltonian in perturbation theory. This formalism was transferred to STM by Tersoff and Hamann [Phys. Rev. Lett. 50, 1998 (1983); Phys. Rev. B 31, 805 (1985)].

This yields an expression for the tunnel current:

$$I \propto V \cdot N_{\text{tip}}(E_F) \cdot N_{\text{sample}}(\vec{r}_0, E_F) \quad (7.30)$$

where the tunnelling tip is approximated as a (metallic) s-orbital, and $N_{\text{tip}}(E_F)$ is the density of states of the tip at the Fermi level E_F , while $N_{\text{sample}}(\vec{r}_0, E_F)$ is the density of states of the sample surface (at E_F) at the position \vec{r}_0 of the tip.

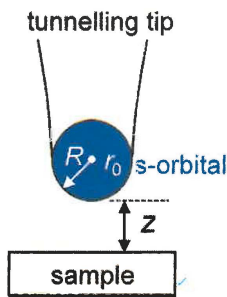


Fig. 7.28: Schematic representation of the tunnelling geometry within the Tersoff-Hamann model [R. Waser (Ed.), Advanced Electronic Materials and Novel Devices, Wiley-VCH, Weinheim (2003); ch. 12].

Here, the **approximation** $eV \ll \phi$ holds,
with ϕ = work function = difference between vacuum level and E_F = barrier height
⇒ at low V STM images the electronic density of states $N_{\text{sample}}(E_F)$!

The atoms are therefore not imaged directly; also N_{tip} influences the image formation, which is often not exactly known. The quality of the tip is thus very important for atomic resolution.

For high spatial resolution, a nano-tip at the lower end of the probe is sufficient that is only 0.1 nm closer to the sample than the rest of the tip, and which therefore dominates the tunnel current I .

Besides the spatial distribution of the densities of state, STM also yields their energy dependence. This follows from measurements of the current-voltage-characteristics, or rather their derivative, the **differential conductance** dI/dV . Approximately,

$$N_{\text{sample}}(eV) \propto \frac{dI}{dV}(V) \quad (7.31)$$

Experimental operating modes of STM:

- Constant height mode: scan of the sample at a constant height z , \rightarrow imaging the tunnel current $I(x, y)$
- Constant current mode: with the help of a feedback loop, z is varied such that $I = \text{const.}$ (via a piezo voltage V_{piezo}) \rightarrow representation of the piezo voltage $V_{\text{piezo}}(x, y)$

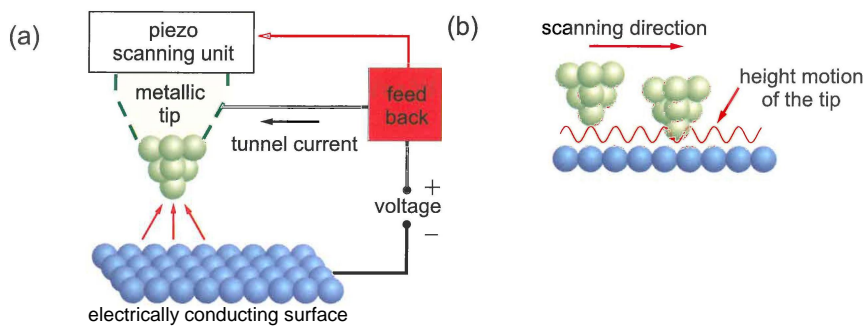


Fig. 7.29: Schematic of STM with a feedback loop [R. Waser (Ed.), Advanced Electronic Materials and Novel Devices, Wiley-VCH, Weinheim (2003); ch. 12].

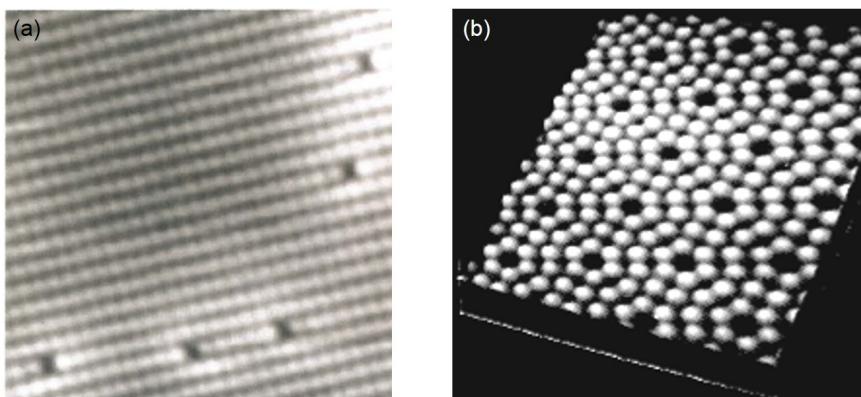


Fig. 7.30: (a) STM image of phosphor defects on an n -doped InP(110) surface; (b) STM image of a Si(111) 7×7 surface [R. Waser (Ed.), Advanced Electronic Materials and Novel Devices, Wiley-VCH, Weinheim (2003); ch. 12].

b) Atomic Force Microscopy (AFM)

AFM is the most widely used scanning probe technique.

In AFM the force between a tip and a surface is detected. The tip is positioned on a flexible cantilever, see Fig. 7.31.

The tip is scanned (with the help of a piezo element) across the surface at a very low distance. → Measurement of the deflection of the cantilever as a function of (x, y). Si or SiN cantilevers with tip radii down to less than 5 nm and spring constants of $k \approx 0.1$ to 10 N/m are commercially available.

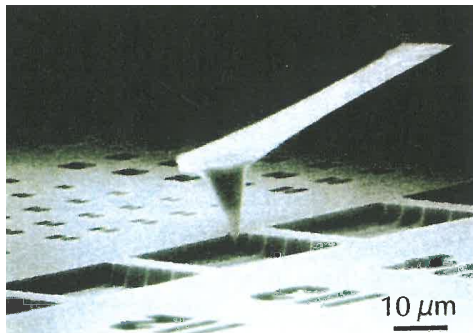


Fig. 7.31: SEM image of a Si cantilever [R. Waser (Ed.), Advanced Electronic Materials and Novel Devices, Wiley-VCH, Weinheim (2003); chap. 12].

Detection of deflection:

The most common technique is optical readout with a laser, which is reflected from the cantilever backside, see Fig. 7.32. The deflection of the laser beam is read out by a 4-segment-photodiode. The difference signal between the upper and lower diode, respectively the left and the right diode, is detected. Vertically, the bending of the cantilever and laterally its torsion (rotation) is measured.

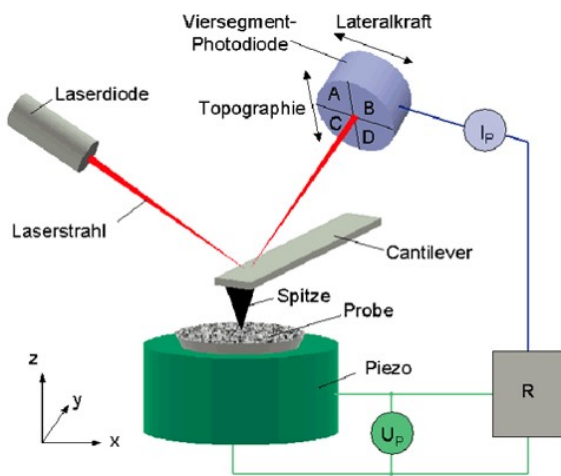


Fig. 7.32: Schematic of AFM with detection by laser reflection [<http://www.chem.sci.gu.edu.au>].

Imaging modes:

AFM can be carried out in various environments, e.g. in air or in liquids. Possible samples are insulators, organic materials, biological macromolecules, polymers, ceramics, glasses, etc. This means that AFM is extremely flexible, allowing for a broad range of possible applications.

With different atomic force microscopy types different types of forces can be analyzed.

In **non-contact mode** the scanning takes place at a distance of $\approx 1 \text{ nm}$: van der Waals, electrostatic, magnetic, capillary forces...

In **contact mode** the tip is brought into direct contact with the surface. Here, ionic, repulsive forces are dominant.

In the **dynamic operating mode** the cantilever is excited close to its resonance frequency $\omega_0 \propto \sqrt{k}$ (k : spring constant). Upon an approach of the tip to the surface, the van der Waals interaction causes a change of k and therefore a shift $\Delta\omega$ of the resonance frequency to lower frequencies.

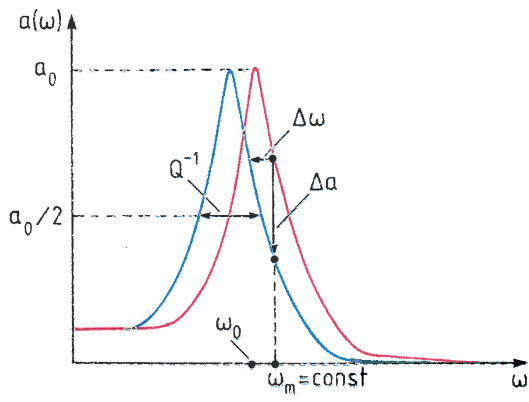


Fig. 7.33: Resonance curves of the tip with and without interaction with a van der Waals potential. Interaction causes a shift $\Delta\omega$ of the resonance frequency, whereby the amplitude $a(\omega)$ of a tip that is excited with ω_m is reduced by $\Delta a(\omega)$ [R. Waser (Ed.), Wiley-VCH (2003); chap. 12].

Upon excitation with $\omega_m > \omega_0$ the oscillation amplitude $a(\omega)$ is reduced by Δa when approaching a surface, since the interaction increases.

Cantilevers with small damping $1/Q$ (Q : quality factor) result in a steep resonance curve and therefore a strong change in Δa for a given frequency shift $\Delta\omega$.

With amplitudes of $a \sim 1 \text{ nm}$ and a measuring accuracy of 1%, changes in the deflection of 0.01 nm have to be detected!

If the feedback loop is used to regulate to a constant oscillation amplitude $a = \text{const}$, images of constant force are obtained.

Forces:

In AFM the van der Waals forces of the attractive interaction between tip and surface (induced dipole-dipole-interaction) are used.

Interaction between two atoms:

- Lennard-Jones-potential $U \propto 1/d^6$ for small distances
- for larger distances: retardation effects, $U \propto 1/d^7$

However: the interaction is not limited to only one atom in the tip and at the surface; the distance dependence of the potential $U(d)$ depends on the geometry. Often the model of a sphere with radius R at a distance d from a half-space with the material-dependent Hamaker-constant A is used, yielding: $U = -\frac{AR}{6} \cdot \frac{1}{d}$.

This results in a significantly weaker distance dependence and a distinctly lower sensitivity compared to STM.

In order to characterize the forces, **force-distance curves** as shown in Fig. 7.34 are recorded at fixed positions (x, y). Upon approaching the surface, at first no effect of the force is observed. As soon as the force becomes noticeable, the cantilever is bent towards the surface (*snap-in*) until the tip is in contact. When the cantilever is further approached, the tip is bent upwards linearly to the cantilever-surface-distance. While retracting the cantilever from the surface, the tip remains in contact until the force no longer prevails and the cantilever snaps back to the parallel position. From the force-distance curve, important information on the resonance frequency of the cantilever and the physical properties of the surface can be gained.

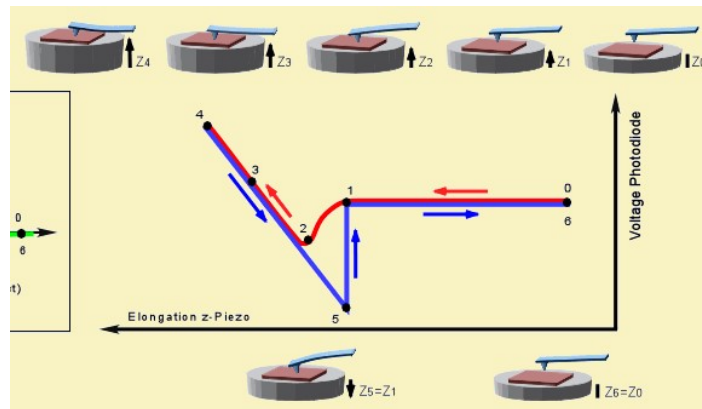


Fig. 7.34: Force-distance curve for approach of the cantilever to the surface and subsequent retraction [http://www3.physik.uni-greifswald.de].

Applications:

- Atomic Force Microscopy (AFM): Most common application, for chemically homogeneous surfaces and van der Waals interactions only: → **surface topography**
- For perfectly flat surfaces from different materials: differences in the Hamaker-constant → **material contrast**
- Magnetic Force Microscopy (MFM): magnetic force between tip with magnetization \vec{M}_{tip} and magnetic scattering field \vec{H}_{sample} of the sample, → image of **magnetic domain structures**, e.g. for data storage media
- Electrostatic Scanning Force Microscopy (EFM) with insulating tip, → detection of the **Coulomb force**, images of surface charges and surface potentials

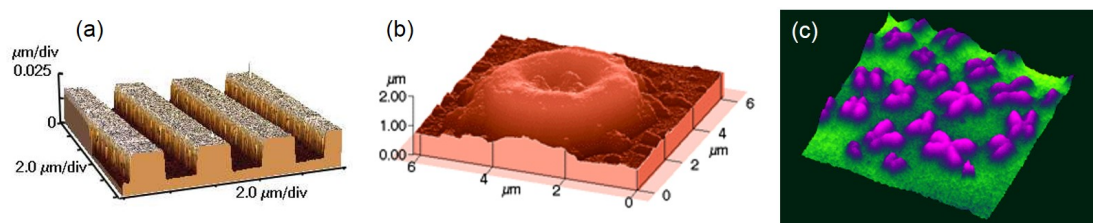


Fig. 7.35: AFM images: (a) lithographic grating, (b) red blood cell, (c) human chromosome [lecture of M. Meyappan, http://www.eng.yale.edu; S. Zhou and M. Farzan, Arizona State University; Digital Instruments].

c) Scanning near-field microscopy (SNOM)

In optical near-field microscopy (Europe: SNOM, US: NSOM) light is focussed at the probe tip.

In **aperture probes** light is guided or detected by metal-covered fibre-tips, whose tips are prepared with an opening of ~ 100 nm diameter. The focus is therefore no longer diffraction-limited, but depends on the diameter of the opening (see fig. 7.36).

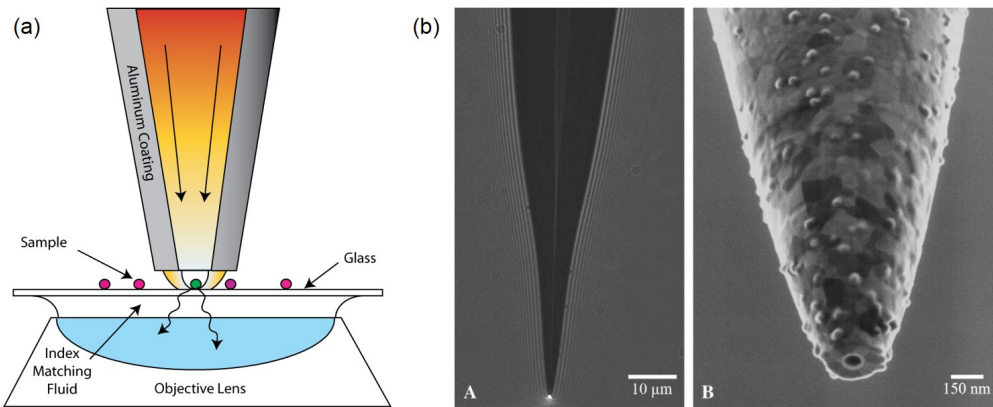


Fig. 7.36: (a) Schematic of the aperture-SNOM, (b) aperture probe with light spot at the tip and SEM image of the opening at a metallized fibre tip [http://ansom.research.pdx.edu; O.L. Mooren et al., JALA 11, 268 (2006)].

In **aperture-less SNOM** massive metal tips (usually gold or silver), or metal nano-structures at the apex of dielectric probes are employed, whose tips are illuminated with a laser. This way, plasmons are excited within the metal (see chap. 7) whereby the light is focussed to a spot with the dimensions of the tip radius (see Fig. 7.37).

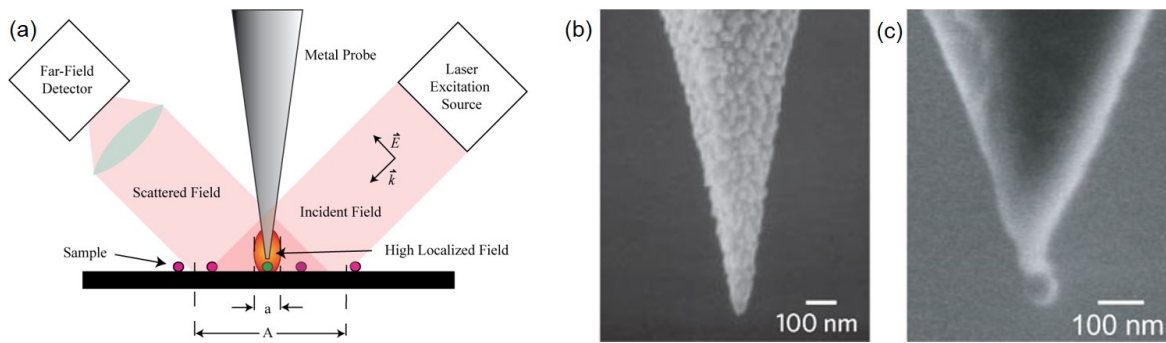


Fig. 7.37: (a) Schematic of aperture-less SNOM, (b) aperture-less metal tip, (c) dielectric tip with metal particle [Nature Photonics 3, 388 (2009); www.pdx.edu/nano-development-lab/tenom-tip-enhanced-near-field-optical-microscopy].

By avoiding the diffraction limit, lateral resolutions on the order of 10 nm can be reached with SNOM.

The light spot interacts with the surface. The optical properties of the surface or rather the electric near-fields created at the surface, are imaged.

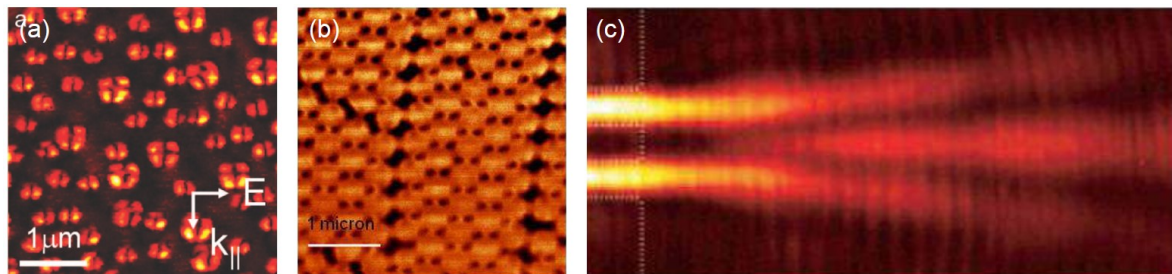


Fig. 7.38: SNOM images: (a) gold discs with dipolar or quadrupolar excitation; (b) honeycomb pattern of Al nano-triangles (dark); (c) SNOM image of surface plasmons in an optical double-slit experiment [R. Esteban et al., Nano Lett. 8, 3155 (2008); Webinar, <http://www.witec.de>; R. Zia et al., Nature Nanotechnol. Lett.].

Besides optical near-field microscopy, the SNOM probe can also be used for *tip-enhanced Raman spectroscopy* (TERS). Here, the local electric near-field E_{nf} at a tip that is illuminated with an external electric field E_0 is used in order to excite a high Raman signal with intensity $I_{TERS} \propto (E_{nf}/E_0)^4$. By point-wise spectroscopy of the surface, it is also possible to record a "Raman-map", which yields detailed information on the chemical composition of the surface. The resolution here is in the range of few nanometers, and therefore clearly better than the resolution of confocal micro-Raman-spectroscopy, see Fig. 7.39.

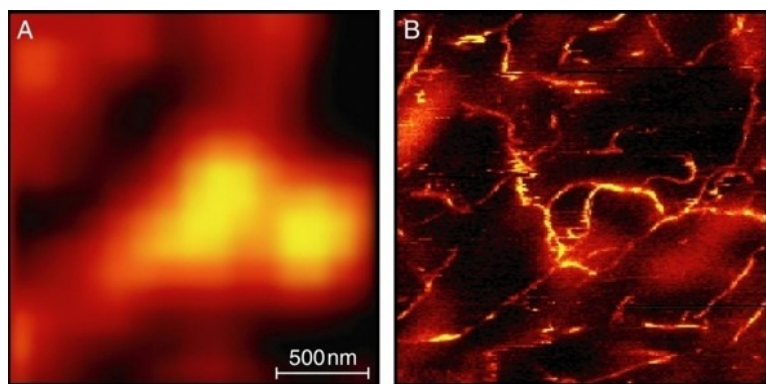


Fig. 7.39: Comparison of (A) a confocal image of a carbon nanotube and (B) a hyper-spectral TERS image of the same sample area, where the signal of a characteristic Raman line of the carbon spectrum is plotted [AG L. Novotny, University of Rochester].

This spectroscopy technique, where the measured intensity is split up into an energy-dependent spectrum, is directly related to further spectroscopy techniques as discussed in the spectroscopy section.

7.3 Spectroscopy

7.3.1 Concepts

There are numerous ways to characterize thin films and nanostructures by spectroscopy. Essentially all conventional spectroscopic techniques can be applied, i.e. the same as discussed in BM KoMa (since there was not much time to discuss these in detail, we refer to specialized courses).

Generally, essentially all types of excitations can be probed, provided that the signal is sufficient, which may be a challenge for some nanostructures with small quantities of material.

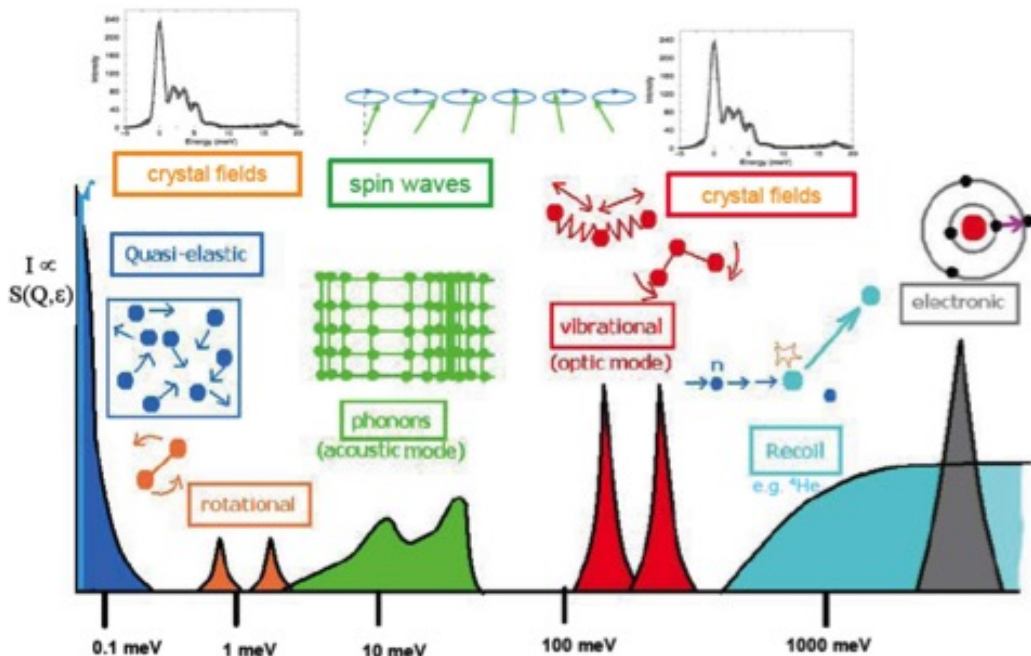


Fig. 7.40: Overview of spectral regions for excitations in condensed matter. Well above 1000 meV of course there are still further transitions related to excitations in the visible, UV, or X-ray regime.

These excitations can be addressed with different probes, e.g.

- photons (in principle in the entire electromagnetic spectrum, including X-rays)
- electrons
- neutrons
- helium atoms

Penetration depth and surface sensitivity

The above probes are similar to section 7.1 (Scattering), including the issue of penetration and information depth, but in the context of spectroscopy we have the important difference that of course by definition the energy of the beam will change in the inelastic (spectroscopic) process, and we may even have a conversion of light into electrons (photoelectron spectroscopy; light in, electron out). For photoelectron spectroscopy, even if the exciting X-rays as the incoming beam have a higher penetration depth, the information depth is determined by the mean free path of the outgoing electrons, which is typically only a few atomic layers (see Figure 7.41).

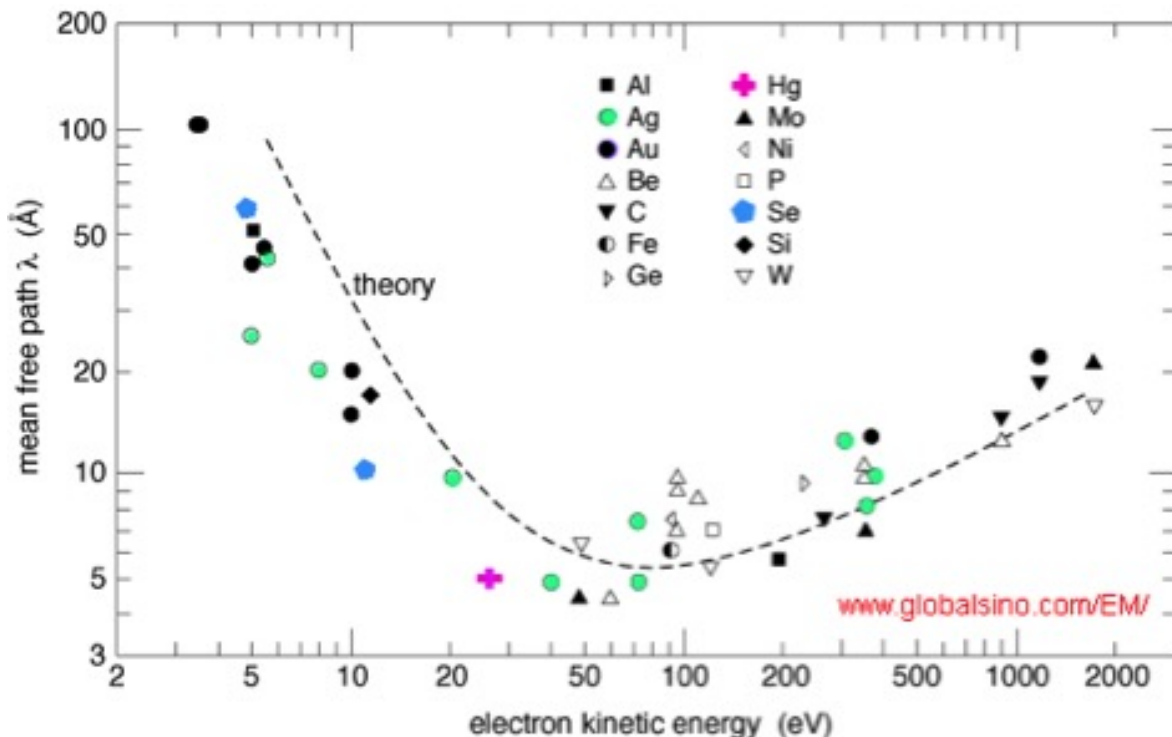


Fig. 7.41: Inelastic mean free path of electrons in a solid, relevant e.g. for photoelectron spectroscopy.

7.3.2 Examples

In the context of this lecture, it is virtually impossible to provide a complete or even only approximately fair account of the numerous types of spectroscopic studies of nanostructures. We will not attempt to summarize all of these here, but rather refer to the selected examples provided in the appendix (pdf of PowerPoint slides). Furthermore, we mention some techniques specific for nanostructures and thin films.

First of all, in particular for nanostructures, the combination of spectroscopy with microscopic information ('spectro-microscopy') is particularly appealing, e.g. to obtain spectroscopic information from one specifically selected nanoparticle or other nanostructure.

Second, similar to Sec. 7.1 (Scattering) time-resolved techniques are of particular interest, and 'beam-in-beam-out' techniques usually do not interfere with other processes on

the surface (chemical reactions; growth processes), which makes them highly suitable for '*in situ*' and real-time observations.

As an example, we shall mention 'differential reflectance spectroscopy' (DRS), which is very efficient for the detection of spectral changes of a film during growth. DRS simply measures the change of the reflected light R (spectrally resolved) relative to the reflection from the substrate R_s as a function of time during growth

$$\frac{\Delta R}{R} = \frac{R - R_s}{R_s} \quad (7.32)$$

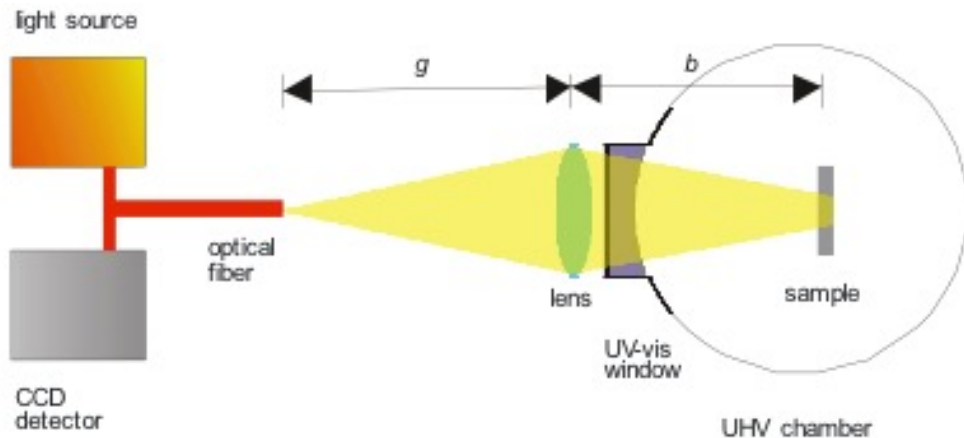


Fig. 7.42: Setup of DRS

The data analysis of DRS is rather straight-forward and particularly simple for the following assumptions

- thin film limits $d \ll \lambda$
- transparent substrate
- angle of incidence ($\text{AOI} = 0^\circ$)

when the signal is directly proportional to the absorption spectrum of the film ($\varepsilon_2(\lambda)$) and its changes during growth

$$\frac{\Delta R}{R} = \frac{8\pi d}{\lambda} \frac{\varepsilon_2}{1 - n_{substrate}^2} \quad (7.33)$$

